

# Construction of 3D Electronic/Ionic Conduction Networks for All-Solid-State Lithium Batteries

Hongli Wan, Liangting Cai, Fudong Han, Jean Pierre Mwizerwa, Chunsheng Wang,\* and Xiayin Yao\*

High and balanced electronic and ionic transportation networks with nanoscale distribution in solid-state cathodes are crucial to realize high-performance all-solid-state lithium batteries. Using  $\text{Cu}_2\text{SnS}_3$  as a model active material, such a kind of solid-state  $\text{Cu}_2\text{SnS}_3$ @graphene- $\text{Li}_7\text{P}_3\text{S}_{11}$  nanocomposite cathodes are synthesized, where 5–10 nm  $\text{Cu}_2\text{SnS}_3$  nanoparticles homogeneously anchor on the graphene nanosheets, while the  $\text{Li}_7\text{P}_3\text{S}_{11}$  electrolytes uniformly coat on the surface of  $\text{Cu}_2\text{SnS}_3$ @graphene composite forming nanoscaled electron/ion transportation networks. The large amount of nanoscaled triple-phase boundary in cathode ensures high power density due to high ionic/electronic conduction and long cycle life due to uniform and reduced volume change of nano- $\text{Cu}_2\text{SnS}_3$ . The  $\text{Cu}_2\text{SnS}_3$ @graphene- $\text{Li}_7\text{P}_3\text{S}_{11}$  cathode layer with  $2.0 \text{ mg cm}^{-2}$  loading in all-solid-state lithium batteries demonstrates a high reversible discharge specific capacity of  $813.2 \text{ mAh g}^{-1}$  at  $100 \text{ mA g}^{-1}$  and retains  $732.0 \text{ mAh g}^{-1}$  after 60 cycles, corresponding to a high energy density of  $410.4 \text{ Wh kg}^{-1}$  based on the total mass of  $\text{Cu}_2\text{SnS}_3$ @graphene- $\text{Li}_7\text{P}_3\text{S}_{11}$  composite based cathode. Moreover, it exhibits excellent rate capability and high-rate cycling stability, showing reversible capacity of  $363.5 \text{ mAh g}^{-1}$  at  $500 \text{ mA g}^{-1}$  after 200 cycles. The study provides a new insight into constructing both electronic and ionic conduction networks for all-solid-state lithium batteries.

are considered to be one of the most promising solid-state electrolytes due to high ionic conductivity and excellent processability as well as low elastic modulus.<sup>[5–9]</sup> The high ionic conductivities of glass-ceramic sulfide electrolytes such as  $\text{Li}_{10}\text{GeP}_2\text{S}_{12}$  ( $1.2 \times 10^{-2} \text{ S cm}^{-1}$ ),<sup>[8]</sup>  $\text{Li}_7\text{P}_3\text{S}_{11}$  ( $1.7 \times 10^{-2} \text{ S cm}^{-1}$ ),<sup>[5]</sup> and  $\text{Li}_{9.54}\text{Si}_{1.74}\text{P}_{1.44}\text{S}_{11.7}\text{Cl}_{0.3}$  ( $2.5 \times 10^{-2} \text{ S cm}^{-1}$ )<sup>[9]</sup> are comparable with that of the liquid carbonate electrolytes. However, the electrochemical performance of all-solid-state lithium batteries using sulfide electrolytes is still inferior to that of commercial liquid electrolyte based lithium-ion batteries. The challenges are attributed to (1) poor electronic/ionic conduction networks in cathodes due to the limited triple solid–solid contact interface and the poor interface compatibility, and (2) high stress/strain due to volume change of active materials and immobile/incompressible solid electrolytes.<sup>[10–12]</sup>

Among all cathode materials, transition-metal sulfides have been considered the most promising cathodes for high-performance all-solid-state lithium batteries because they (1) show better interface compatibility with sulfide electrolytes than lithium transition-metal oxides, (2) have higher energy density and higher chemical stability than lithium transition-metal oxides,<sup>[13–16]</sup> and (3) possess better electronic conductivity and electrochemical stability than  $\text{Li}_2\text{S}$  and sulfur.<sup>[17–20]</sup> However, the poor electronic/ionic conduction network and continuously increased solid–solid contact interface resistance during charge/discharge cycles are still challenges for solid-state transition-metal sulfide cathodes. One promising strategy is to coat nanosized transition-metal sulfides onto highly conductive carbonaceous materials to enhance the electronic conductivity.<sup>[21–23]</sup> The thickness of transition-metal sulfide should be less than few nanometers to reduce the stress/strain and interface resistance, and to allow the electrons conduction across the transition-metal sulfide nanolayer through tunnel effect to solid electrolyte for charge transfer reaction. The long cycle life of such *active material/electron additive* nanocomposite cathodes was demonstrated by us using nanolayer  $\text{Cu}_2\text{ZnSnS}_4$  (or sulfur) deposited graphene as model cathodes.<sup>[21,24]</sup> The  $\text{Cu}_2\text{ZnSnS}_4$ /graphene nanocomposite prepared using hydrothermal approach shows a discharge capacity of  $645.4 \text{ mAh g}^{-1}$  after 50 cycles at  $50 \text{ mA g}^{-1}$ .<sup>[21]</sup>

## 1. Introduction

All-solid-state lithium batteries using nonflammable inorganic solid electrolytes have attracted increasing attention due to its high safety and reliability.<sup>[1–4]</sup> Sulfide electrolytes

H. Wan, L. Cai, J. P. Mwizerwa, Prof. X. Yao  
Ningbo Institute of Materials Technology and Engineering  
Chinese Academy of Sciences  
Ningbo 315201, P. R. China  
E-mail: yaoxy@nimte.ac.cn

H. Wan, J. P. Mwizerwa, Prof. X. Yao  
Center of Materials Science and Optoelectronics Engineering  
University of Chinese Academy of Sciences  
Beijing 100049, P. R. China

Dr. F. Han, Prof. C. Wang  
Department of Chemical and Biomolecular Engineering  
University of Maryland  
College Park, MD 20742, USA  
E-mail: cswang@umd.edu

The ORCID identification number(s) for the author(s) of this article can be found under <https://doi.org/10.1002/smll.201905849>.

DOI: 10.1002/smll.201905849

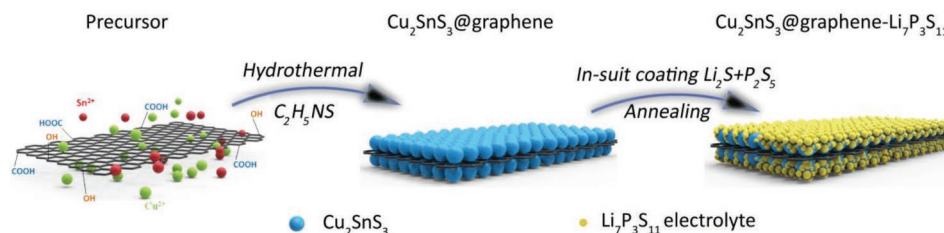


**Figure 1.** Schematic illustration of the fabrication procedure of  $\text{Cu}_2\text{SnS}_3$ @graphene- $\text{Li}_7\text{P}_3\text{S}_{11}$  nanocomposite, where hydrothermal method was applied to synthesize  $\text{Cu}_2\text{SnS}_3$ @graphene composite and then  $\text{Li}_7\text{P}_3\text{S}_{11}$  electrolyte was coated on  $\text{Cu}_2\text{SnS}_3$ @graphene by an in situ liquid-phase reaction followed by an annealing treatment.

while 2 nm S-coated graphene can maintain a high and reversible capacity of  $830 \text{ mAh g}^{-1}$  at 1.0 C for 750 cycles,<sup>[24]</sup> However, the ionic conduction of *active material/electron additive* is still a challenge due to poor contact between active materials with electrolyte, which limits the further enhancement of the electrochemical performance. To enhance the ionic conduction of cathode, we coated a thin layer of electrolyte onto active materials nanosheet to form *active materials/electrolyte* nanocomposite. All-solid-state lithium batteries employing cobalt sulfide- $\text{Li}_7\text{P}_3\text{S}_{11}$  nanocomposites in combination with the  $\text{Li}_7\text{P}_3\text{S}_{11}$  electrolyte and Super P as the cathode and lithium metal as the anode showed reversible discharge capacity of  $421 \text{ mAh g}^{-1}$  at  $1.27 \text{ mA cm}^{-2}$  after 1000 cycles.<sup>[25]</sup> However, the *poor electronic conduction in active materials/electrolyte nanocomposite* cathode limits the electrochemical performance. Here, we reported a comprehensive strategy to simultaneously enhance both ionic and electronic conduction by formation of nanoscaled 3D electronic/ionic conduction networks in cathode. Use of  $\text{Cu}_2\text{SnS}_3$  as a model active material, we first coated 5–10 nm  $\text{Cu}_2\text{SnS}_3$  nanoparticles onto graphene to ensure high electronic conduction, and then coated additional sulfide electrolyte layer/particle to form nanoscaled 3D electronic/ionic networks (Figure 1). Such a solid-state nanocomposite cathode structure is similar to porous sulfide nanocomposite cathodes in liquid electrolyte. Due to immobility of solid sulfide electrolytes, the transition-metal sulfide nanoparticles anchored on graphene can effectively reduce the stress/strain and achieve a good electronic conduction. The thin electrolyte layer coating on nano-active material/graphene composite play a critical role in establishing the 3D ionic conduction network for high power density and long cycle life.

The reason to select copper tin sulfide ( $\text{Cu}_2\text{SnS}_3$ ) as a model active cathode material is because it has a higher electrical conductivity than other copper-based multicomponent chalcogenide,<sup>[26,27]</sup> and higher energy density than reported  $\text{Cu}_2\text{ZnSnS}_4$  in all-solid-state lithium batteries. The low energy density of  $\text{Cu}_2\text{ZnSnS}_4$  is because the alloying reaction of Zn in  $\text{Cu}_2\text{ZnSnS}_4$  begins below 0.5 V<sup>[28]</sup> that is beyond the range of the setting cut-off voltage (0.5–3 V) of  $\text{Cu}_2\text{ZnSnS}_4$  cathodes.

In this work,  $\text{Cu}_2\text{SnS}_3$ @graphene nanocomposite were prepared using a hydrothermal reaction, and then a thin layer of  $\text{Li}_7\text{P}_3\text{S}_{11}$  electrolytes was coated on  $\text{Cu}_2\text{SnS}_3$ @graphene via in situ liquid-phase reaction forming  $\text{Cu}_2\text{SnS}_3$ @graphene- $\text{Li}_7\text{P}_3\text{S}_{11}$  nanocomposites (Figure 1). An all-solid-state lithium battery employing  $\text{Cu}_2\text{SnS}_3$ @graphene- $\text{Li}_7\text{P}_3\text{S}_{11}$  as a cathode material, a lithium metal as an anode and a sulfide

electrolyte bilayer as a solid electrolyte was fabricated and the electrochemical performances of  $\text{Cu}_2\text{SnS}_3$ @graphene- $\text{Li}_7\text{P}_3\text{S}_{11}$ / $\text{Li}_{10}\text{GeP}_2\text{S}_{12}$ /75% $\text{Li}_2\text{S}$ -24% $\text{P}_2\text{S}_5$ -1% $\text{P}_2\text{O}_5$ /Li all-solid-state cell were evaluated and compared to other all-solid-state cells using  $\text{Cu}_2\text{SnS}_3$ ,  $\text{Cu}_2\text{SnS}_3$ @graphene as cathode material. The results prove that the 3D nanoscaled ionic/electronic networks formed by coating electrolytes on active materials/graphene composite can significantly improve the cycling stability and rate capability of all-solid-state lithium batteries. The resultant  $\text{Cu}_2\text{SnS}_3$ @graphene- $\text{Li}_7\text{P}_3\text{S}_{11}$  nanocomposite based cathodes in all-solid-state lithium batteries exhibit capacity of  $732.0 \text{ mAh g}^{-1}$  and  $363.5 \text{ mAh g}^{-1}$  after cycling at  $100 \text{ mA g}^{-1}$  for 60 cycles and  $500 \text{ mA g}^{-1}$  for 200 cycles, respectively.

## 2. Results and Discussion

Figure 2 displays the X-ray powder diffraction (XRD) patterns of  $\text{Cu}_2\text{SnS}_3$ ,  $\text{Cu}_2\text{SnS}_3$ @graphene, and  $\text{Cu}_2\text{SnS}_3$ @graphene- $\text{Li}_7\text{P}_3\text{S}_{11}$  nanocomposite. The main characteristic diffraction peaks of pure  $\text{Cu}_2\text{SnS}_3$  at  $28.6^\circ$ ,  $32.7^\circ$ ,  $47.6^\circ$ , and  $56.7^\circ$  correspond to the diffraction from the (111), (200), (220), and (311) planes of the standard cubic phase  $\text{Cu}_2\text{SnS}_3$  (JCPDS card no. 01-089-2877).<sup>[26]</sup> The obtained  $\text{Cu}_2\text{SnS}_3$ @graphene and  $\text{Cu}_2\text{SnS}_3$ @graphene- $\text{Li}_7\text{P}_3\text{S}_{11}$  nanocomposite show similar XRD patterns to that of  $\text{Cu}_2\text{SnS}_3$ , indicating the introduction of graphene oxide during hydrothermal synthesis process and the electrolyte deposition during in situ liquid-phase reaction

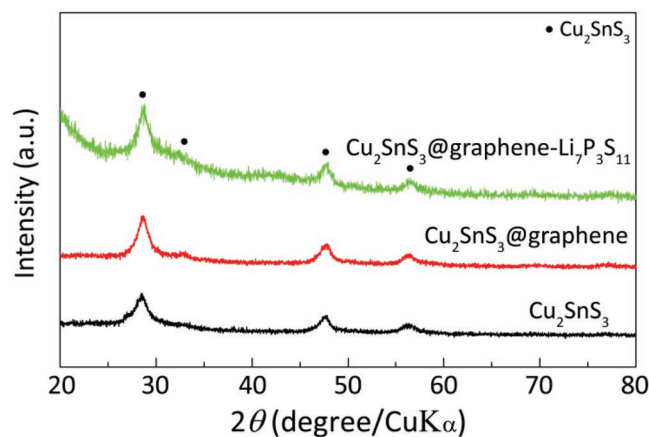


**Figure 2.** XRD patterns of  $\text{Cu}_2\text{SnS}_3$ ,  $\text{Cu}_2\text{SnS}_3$ @graphene, and  $\text{Cu}_2\text{SnS}_3$ @graphene- $\text{Li}_7\text{P}_3\text{S}_{11}$  nanocomposite.

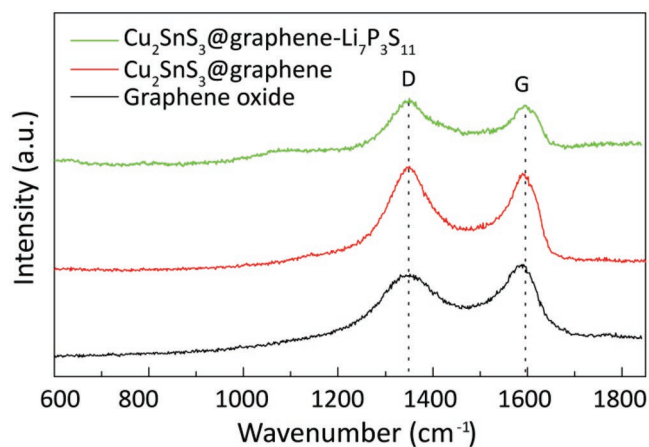


**Figure 3.** Raman spectra of graphene oxide,  $\text{Cu}_2\text{SnS}_3$ @graphene,  $\text{Cu}_2\text{SnS}_3$ @graphene- $\text{Li}_7\text{P}_3\text{S}_{11}$  in the wavelength range of  $600\text{--}1800\text{ cm}^{-1}$ .

do not influence the phase of  $\text{Cu}_2\text{SnS}_3$ . For  $\text{Cu}_2\text{SnS}_3$ @graphene- $\text{Li}_7\text{P}_3\text{S}_{11}$  nanocomposite, no obvious peaks related to graphene and electrolyte are observed, which might be due to the low amount of graphene and electrolyte in the nanocomposites. The amount of graphene in the  $\text{Cu}_2\text{SnS}_3$ @graphene can be determined by carbon sulfur analyses and the results reveal that the graphene content in the as-prepared  $\text{Cu}_2\text{SnS}_3$ /graphene is about 9.6%. The reduction of graphene oxide during hydrothermal reaction was confirmed by Raman spectroscopy, as shown in **Figure 3**. Two peaks at about  $1350$  and  $1592\text{ cm}^{-1}$  are observed, which attributes to the D and G bands from graphene. The peak at about  $1592\text{ cm}^{-1}$  (G band) is related to the vibration of the  $sp^2$ -banded carbon atoms in a 2D hexagonal lattice, while the peak at about  $1350\text{ cm}^{-1}$  (D band) is related to the defects and disorder in hexagonal graphitic layers.<sup>[29]</sup> The intensity ratio ( $I_D/I_G$ ) of the D band to G band was 1.027 for  $\text{Cu}_2\text{SnS}_3$ /graphene that is high than that of graphene oxide ( $I_D/I_G = 0.911$ ), due to reduction of graphene oxide during hydrothermal reaction<sup>[27,30]</sup> and decrease in the average size of the  $sp^2$  domains.<sup>[29,31]</sup> After coating  $\text{Cu}_2\text{SnS}_3$ @graphene with  $\text{Li}_7\text{P}_3\text{S}_{11}$  electrolyte, the intensity ratio ( $I_D/I_G$ ) of the D band to G band (1.024) for  $\text{Cu}_2\text{SnS}_3$ @graphene- $\text{Li}_7\text{P}_3\text{S}_{11}$  nanocomposite is similar to that of  $\text{Cu}_2\text{SnS}_3$ @graphene, suggesting that the introduction of electrolytes does not change the electronic conduction property of graphene.

The morphology of three  $\text{Cu}_2\text{SnS}_3$  cathode materials was observed using a scanning electron microscope (SEM). As shown in **Figure 4**, the pure  $\text{Cu}_2\text{SnS}_3$  has particle size of  $5\text{--}10\text{ nm}$  and obvious aggregations. However, the  $\text{Cu}_2\text{SnS}_3$  nanoparticles in  $\text{Cu}_2\text{SnS}_3$ @graphene composite anchor homogeneously on the graphene nanosheets without aggregation. After  $\text{Li}_7\text{P}_3\text{S}_{11}$  coating on the  $\text{Cu}_2\text{SnS}_3$ @graphene, more particles are distributed on the graphene nanosheets, which implies that  $\text{Li}_7\text{P}_3\text{S}_{11}$  are deposited on the surface of  $\text{Cu}_2\text{SnS}_3$ @graphene forming  $\text{Cu}_2\text{SnS}_3$ @graphene- $\text{Li}_7\text{P}_3\text{S}_{11}$  nanocomposite.

More detailed morphology and structure analysis of  $\text{Cu}_2\text{SnS}_3$ ,  $\text{Cu}_2\text{SnS}_3$ @graphene and  $\text{Cu}_2\text{SnS}_3$ @graphene- $\text{Li}_7\text{P}_3\text{S}_{11}$  nanocomposites were further conducted using transmission electron microscope (TEM) and high-resolution transmission electron

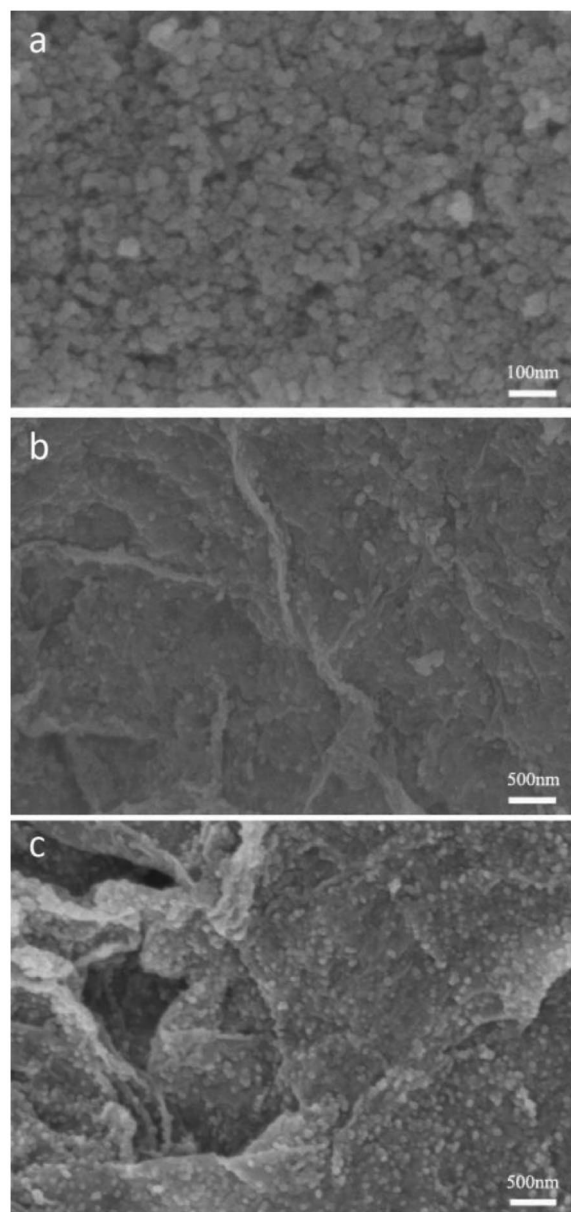


**Figure 4.** SEM images of a)  $\text{Cu}_2\text{SnS}_3$  nanoparticles, b)  $\text{Cu}_2\text{SnS}_3$ @graphene composite, and c)  $\text{Cu}_2\text{SnS}_3$ @graphene- $\text{Li}_7\text{P}_3\text{S}_{11}$  composite.

microscopy (HRTEM). As shown in **Figure 5**, the pure  $\text{Cu}_2\text{SnS}_3$  nanoparticles (Figure 5a) with a particle size distribution of  $5\text{--}10\text{ nm}$  aggregate into a large secondary particles, while the  $\text{Cu}_2\text{SnS}_3$  nano-particles in  $\text{Cu}_2\text{SnS}_3$ @graphene (Figure 5c) and in  $\text{Cu}_2\text{SnS}_3$ @graphene- $\text{Li}_7\text{P}_3\text{S}_{11}$  nanocomposite (Figure 5e) distribute homogeneously on graphene nanosheets without aggregation, which is in accordance with the SEM results. These results imply that the presence of graphene will restrict aggregation of nanoparticles during the hydrothermal process. In the HRTEM images of  $\text{Cu}_2\text{SnS}_3$  (Figure 5b),  $\text{Cu}_2\text{SnS}_3$ @graphene (Figure 5d), and  $\text{Cu}_2\text{SnS}_3$ @graphene- $\text{Li}_7\text{P}_3\text{S}_{11}$  (Figure 5f), the lattice fringe of about  $0.314\text{ nm}$  corresponds to the  $(-2\ -1\ 1)$  lattice plane of triclinic  $\text{Cu}_2\text{SnS}_3$  structure<sup>[27]</sup> and the  $0.299\text{ nm}$  can be indexed to  $(3\ 1\ 1)$  lattice plane of crystal

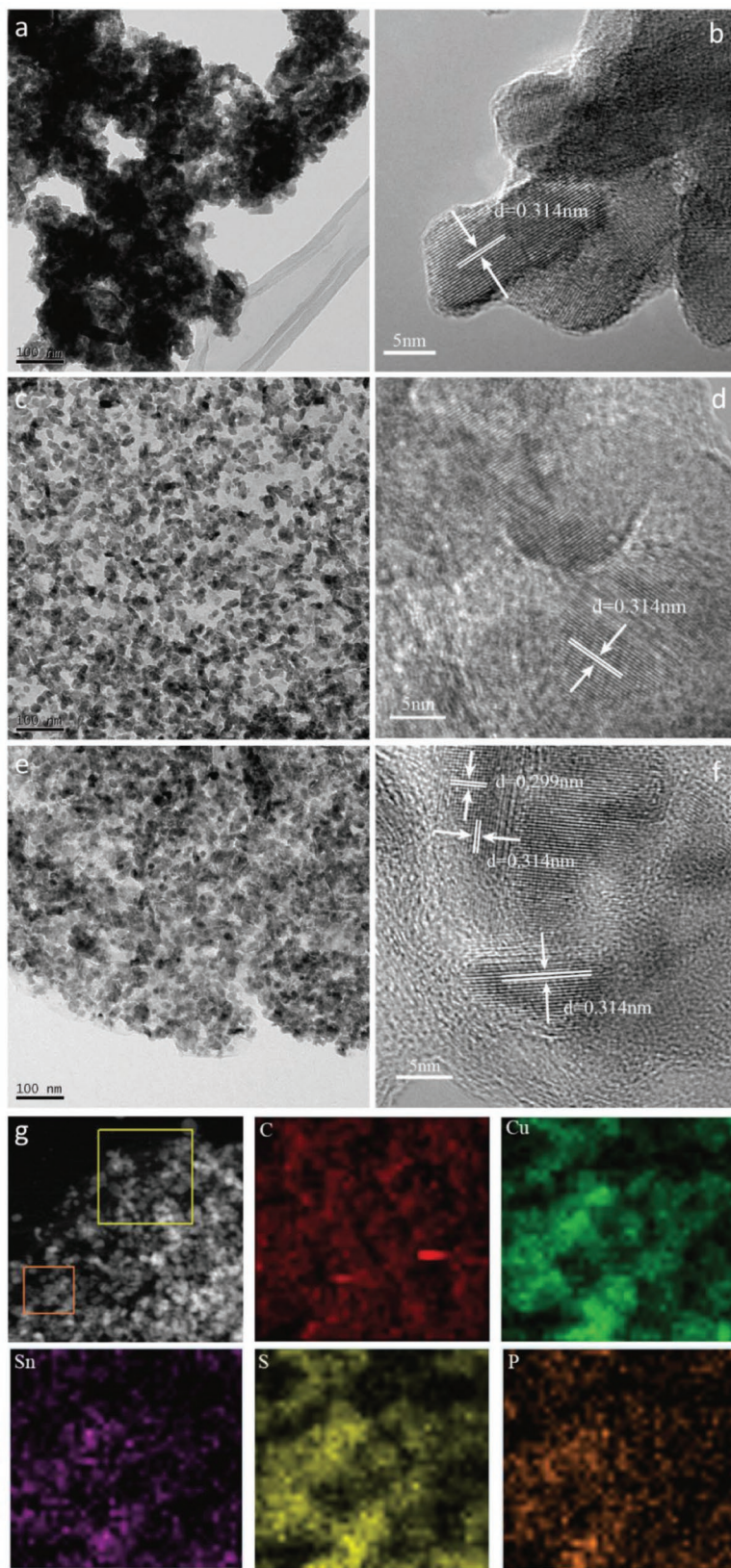


**Figure 5.** TEM and HRTEM images of a,b) Cu<sub>2</sub>SnS<sub>3</sub> nanoparticles, c,d) Cu<sub>2</sub>SnS<sub>3</sub>@graphene, and e,f) Cu<sub>2</sub>SnS<sub>3</sub>@graphene-Li<sub>7</sub>P<sub>3</sub>S<sub>11</sub>. g) STEM elemental mapping images of Cu<sub>2</sub>SnS<sub>3</sub>@graphene-Li<sub>7</sub>P<sub>3</sub>S<sub>11</sub> nanocomposites.

Li<sub>7</sub>P<sub>3</sub>S<sub>11</sub> electrolyte.<sup>[25]</sup> As shown in Figure 5f, the lattice planes of Cu<sub>2</sub>SnS<sub>3</sub> and Li<sub>7</sub>P<sub>3</sub>S<sub>11</sub> are interlaced, suggesting that Cu<sub>2</sub>SnS<sub>3</sub> nanoparticle is partially coated by Li<sub>7</sub>P<sub>3</sub>S<sub>11</sub> electrolyte, demonstrating the successful formation of large amount of nanoscaled 3D triple phase in Cu<sub>2</sub>SnS<sub>3</sub>@graphene-Li<sub>7</sub>P<sub>3</sub>S<sub>11</sub> nanocomposite. These intimate and stable solid-solid contact triple-interfaces between Cu<sub>2</sub>SnS<sub>3</sub> nanoparticles, graphene, and electrolytes will significantly enhance the cycle life and rate performance. Furthermore, the scanning transmission electron microscopy (STEM) element mapping of Cu<sub>2</sub>SnS<sub>3</sub>@graphene-Li<sub>7</sub>P<sub>3</sub>S<sub>11</sub> nanocomposite in Figure 5g also confirms that the Cu<sub>2</sub>SnS<sub>3</sub> nanoparticles were coated with Li<sub>7</sub>P<sub>3</sub>S<sub>11</sub> electrolyte as demonstrated by overlapping of P element with Cu, Sn elements.

The graphene in Cu<sub>2</sub>SnS<sub>3</sub>@graphene and Cu<sub>2</sub>SnS<sub>3</sub>@graphene-Li<sub>7</sub>P<sub>3</sub>S<sub>11</sub> nanocomposites not only enhances the electronic conduction, but also significantly enhances reaction area as demonstrated by the high surface area obtained using Brunauer–Emmett–Teller (BET) nitrogen absorption/desorption measurement. The specific surface area of Cu<sub>2</sub>SnS<sub>3</sub>@graphene is 84.0795 m<sup>2</sup> g<sup>-1</sup>, which is five times higher than that of neat aggregated Cu<sub>2</sub>SnS<sub>3</sub> nanoparticles (17.1361 m<sup>2</sup> g<sup>-1</sup>). The large surface area of Cu<sub>2</sub>SnS<sub>3</sub>@graphene provides more sites for the deposition of Li<sub>7</sub>P<sub>3</sub>S<sub>11</sub> electrolyte during the in situ liquid-phase synthesis of Cu<sub>2</sub>SnS<sub>3</sub>@graphene-Li<sub>7</sub>P<sub>3</sub>S<sub>11</sub> nanocomposite, which is beneficial for the construction of continuous ionic/electronic network. In addition, the introduction of graphene can also accommodate the volume expansion/contraction of active materials during discharge-charge processes, suppressing agglomeration of active materials. Therefore, long cycling stability and high-rate capability are expected for Cu<sub>2</sub>SnS<sub>3</sub>@graphene-Li<sub>7</sub>P<sub>3</sub>S<sub>11</sub> nanocomposite cathodes.

The electrochemical performances of three active material based cathodes (Cu<sub>2</sub>SnS<sub>3</sub>, Cu<sub>2</sub>SnS<sub>3</sub>@graphene, and Cu<sub>2</sub>SnS<sub>3</sub>@graphene-Li<sub>7</sub>P<sub>3</sub>S<sub>11</sub>) were evaluated in all-solid-state lithium cells using cyclic voltammogram (CV). As shown in Figure S1a, Supporting Information, during the first cathodic scan (Li ion insertion) of pure Cu<sub>2</sub>SnS<sub>3</sub> cathode, two broad peaks at 1.881 and 0.907 V are observed, corresponding to the electrochemical reduction of Cu and Sn ions into metallic Cu and Sn nanoparticles. In the first anodic scan, two oxidation peaks at about 1.920 and 2.391 V ascribe to the oxidation reaction of Sn and Cu nanoparticles back to ions.<sup>[21]</sup> After

first lithiation/delithiation activation cycle, the reduction peak at around 1.881 V shift to 1.966 V. The  $\text{Cu}_2\text{SnS}_3$ @graphene (Figure S1b, Supporting Information) and  $\text{Cu}_2\text{SnS}_3$ @graphene- $\text{Li}_7\text{P}_3\text{S}_{11}$  (Figure S1c, Supporting Information) cathodes display an identical electrochemical reaction mechanism as  $\text{Cu}_2\text{SnS}_3$  cathode but have a less polarization between lithiation and delithiation due to the enhanced electronic conductivity for  $\text{Cu}_2\text{SnS}_3$ @graphene cathode and both high ionic and electronic conductivity for  $\text{Cu}_2\text{SnS}_3$ @graphene- $\text{Li}_7\text{P}_3\text{S}_{11}$  cathode. After first activation cycles, the CV curves of all three  $\text{Cu}_2\text{SnS}_3$  cathodes are almost overlapped, indicating the high reversibility of  $\text{Cu}_2\text{SnS}_3$  in the all-solid-state lithium cell.

The first three discharge-charge voltage profiles of pure  $\text{Cu}_2\text{SnS}_3$ ,  $\text{Cu}_2\text{SnS}_3$ @graphene, and  $\text{Cu}_2\text{SnS}_3$ @graphene- $\text{Li}_7\text{P}_3\text{S}_{11}$  in all-solid-state lithium batteries between 0.5 and 3.0 V at the current density of  $100 \text{ mA g}^{-1}$  and room temperature are shown in Figure 6a–c. Three  $\text{Cu}_2\text{SnS}_3$ -based cathodes show similar voltage profiles, where the obvious discharge plateau at around 2.0 V and a slop between 0.9 and 1.5 V derive from the reduction of Cu and Sn species to metallic Cu and Sn, respectively, and the slop between 1.7 and 2.1 V, and a plat plateau at 2.3 V in the charge curves are related to the reversible oxidation reaction of Sn and Cu nanoparticles, respectively, which are in accordance with the results shown in CV

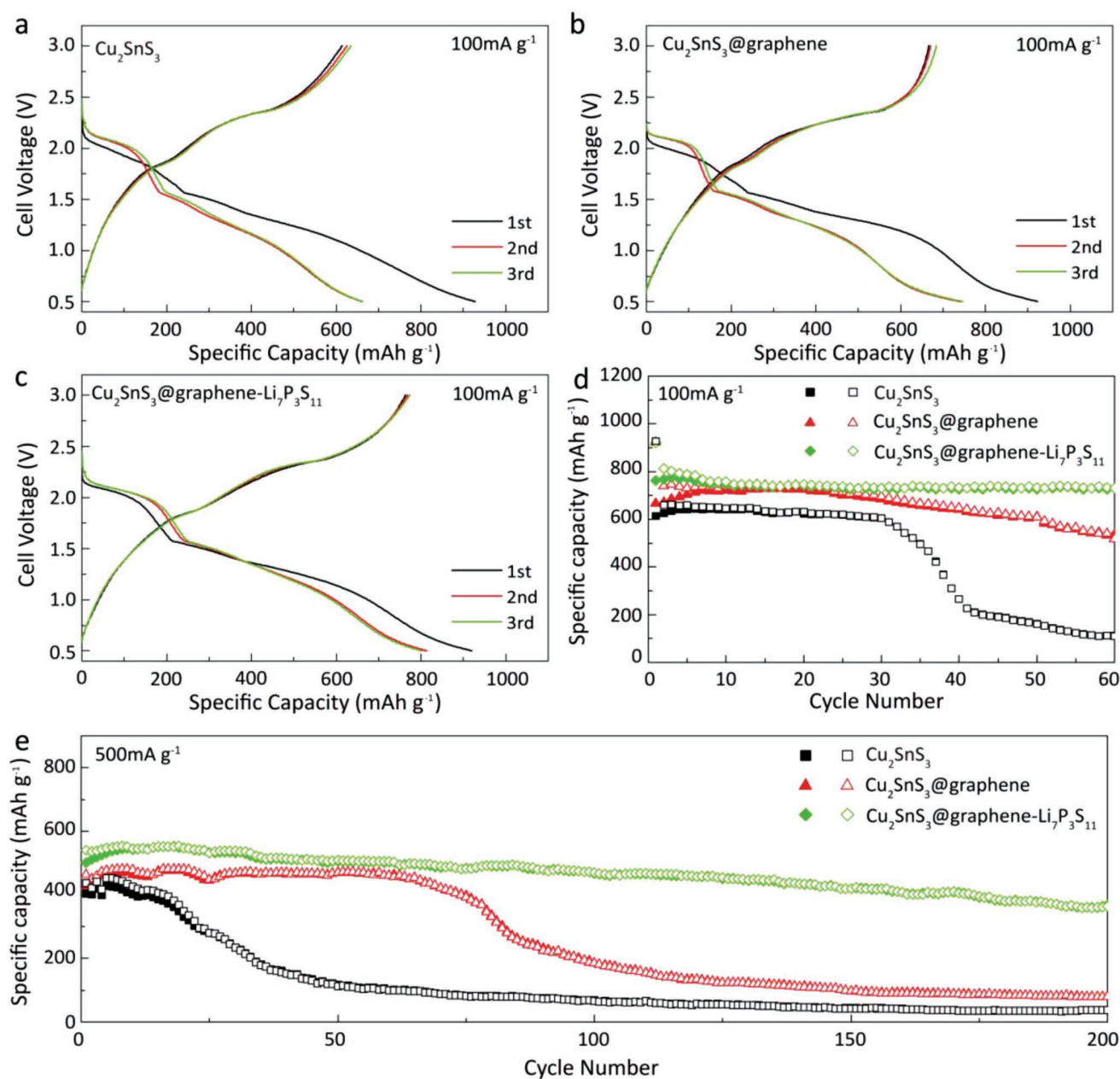


**Figure 6.** Galvanostatic discharge/charge profiles of a) pure  $\text{Cu}_2\text{SnS}_3$  nanoparticles, b)  $\text{Cu}_2\text{SnS}_3$ @graphene, c)  $\text{Cu}_2\text{SnS}_3$ @graphene- $\text{Li}_7\text{P}_3\text{S}_{11}$ . d) Cyclic performance of as-prepared samples under a current density of  $100 \text{ mA g}^{-1}$ . e) High-rate cyclic performance of as-prepared samples at  $500 \text{ mA g}^{-1}$ .

curves (Figure S1, Supporting Information). The first coulombic efficiency of  $\text{Cu}_2\text{SnS}_3$ @graphene- $\text{Li}_7\text{P}_3\text{S}_{11}$  electrode is 82.9%, which is higher than that of pure  $\text{Cu}_2\text{SnS}_3$  (66.1%) and  $\text{Cu}_2\text{SnS}_3$ @graphene (72.2%) cathodes. The low coulombic efficiency for pure  $\text{Cu}_2\text{SnS}_3$  and  $\text{Cu}_2\text{SnS}_3$ @graphene cathodes might be caused by the inferior triple contacts among the discharge products, electrolyte, and electronic additive due to volume expansion of active material after discharge process, leading to electrochemically inaccessibility of partial noncontact discharge products.<sup>[25]</sup> Besides, after the first cycle, the voltage separation between the charge and discharge plateau is the smallest for  $\text{Cu}_2\text{SnS}_3$ @graphene- $\text{Li}_7\text{P}_3\text{S}_{11}$  nanocomposite, suggesting the nanoscaled intimate triple contact structures, where electrochemical reaction occurs, are still well maintained after cycling, further confirming the introduction of both graphene and  $\text{Li}_7\text{P}_3\text{S}_{11}$  electrolyte can increase the reversibility of  $\text{Cu}_2\text{SnS}_3$ . Figure 6d compares the cyclic performance of pure  $\text{Cu}_2\text{SnS}_3$ ,  $\text{Cu}_2\text{SnS}_3$ @graphene, and  $\text{Cu}_2\text{SnS}_3$ @graphene- $\text{Li}_7\text{P}_3\text{S}_{11}$  cathodes at a low current density of  $100 \text{ mA g}^{-1}$ .  $\text{Cu}_2\text{SnS}_3$ @graphene- $\text{Li}_7\text{P}_3\text{S}_{11}$  electrode exhibits a stable capacity of  $732.0 \text{ mAh g}^{-1}$  for 60 cycles, corresponding to a high energy density of  $410.4 \text{ Wh kg}^{-1}$  based on the total mass of cathode layer. However, the discharge specific capacities of  $\text{Cu}_2\text{SnS}_3$ @graphene and  $\text{Cu}_2\text{SnS}_3$  cathodes decreases to  $541.2$  and  $111.8 \text{ mAh g}^{-1}$  after 60 cycles, respectively. The long cycling stability was measured at a high current density of  $500 \text{ mA g}^{-1}$  (Figure 6e). After 200 cycles, the discharge specific capacity of  $\text{Cu}_2\text{SnS}_3$ @graphene- $\text{Li}_7\text{P}_3\text{S}_{11}$  electrode still retains at about  $363.5 \text{ mAh g}^{-1}$ , while the discharge capacities of  $\text{Cu}_2\text{SnS}_3$ @graphene and  $\text{Cu}_2\text{SnS}_3$  cathodes are rapidly decreased to  $78.9$  and  $36.4 \text{ mAh g}^{-1}$ , respectively. These results indicate that  $\text{Cu}_2\text{SnS}_3$ @graphene- $\text{Li}_7\text{P}_3\text{S}_{11}$  nanocomposite cathode has long cycling stability in all-solid-state lithium batteries due to unique cathode architecture with 3D ionic/electronic network and small/uniform volume change.

The rate performances of pure  $\text{Cu}_2\text{SnS}_3$ ,  $\text{Cu}_2\text{SnS}_3$ @graphene, and  $\text{Cu}_2\text{SnS}_3$ @graphene- $\text{Li}_7\text{P}_3\text{S}_{11}$  electrodes were also evaluated. Figure S2, Supporting Information, shows the galvanostatic discharge/charge curves of three  $\text{Cu}_2\text{SnS}_3$ -based cathodes. The  $\text{Cu}_2\text{SnS}_3$ @graphene- $\text{Li}_7\text{P}_3\text{S}_{11}$  nanocomposite can provide discharge specific capacities of  $964.5$ ,  $813.2$ ,  $706.8$ ,  $540.3$ ,  $466.9$ , and  $359.5 \text{ mAh g}^{-1}$  at current densities of  $50$ ,  $100$ ,  $200$ ,  $500$ ,  $1000$ , and  $2000 \text{ mA g}^{-1}$ , respectively, while the  $\text{Cu}_2\text{SnS}_3$ @graphene cathodes can only provide the discharge specific capacities of  $829.7$ ,  $739.5$ ,  $584.5$ ,  $462.5$ ,  $219.5$ , and  $100.5 \text{ mAh g}^{-1}$ , respectively.  $\text{Cu}_2\text{SnS}_3$  cathode shows the worst rate performances with capacities of  $828.1$ ,  $660.6$ ,  $543.1$ ,  $436.3$ ,  $202.8$ , and  $67.2 \text{ mAh g}^{-1}$  at the same step currents, respectively.

To understand the mechanism for superior rate capacity and long cycle stability of the  $\text{Cu}_2\text{SnS}_3$ @graphene- $\text{Li}_7\text{P}_3\text{S}_{11}$  cathodes, the impedance of  $\text{Cu}_2\text{SnS}_3$ @graphene- $\text{Li}_7\text{P}_3\text{S}_{11}$  cathodes at a fully charged state at first and 100 cycles was measured using electrochemical impedance spectroscopy (EIS) and compared them to the impedances of other two cathodes. As shown in Figure S3, Supporting Information, the Nyquist plots mainly consist of ohmic resistance ( $R_e$ ) in the high-frequency range, which stems from the resistance of the electrode and solid electrolyte layers, a compressed semicircle in the middle-frequency region, which corresponds to the charge transfer

resistance ( $R_{ct}$ ), and a sloped line in the low-frequency region, which is related to Li-ion diffusion into the bulk electrode ( $Z_w$ ). Constant phase element (CPE) represents the nonideal capacitance of the double layer. The fitted results obtained from the equivalent circuit model are shown in Table S1, Supporting Information. After the first discharge/charge cycle, the EISs of three cells show a similar slope line, and  $R_e$  values are almost the same due to the employment of the same bilayer electrolyte. After 100 cycles, the  $\text{Cu}_2\text{SnS}_3$ @graphene- $\text{Li}_7\text{P}_3\text{S}_{11}$ /Li cell shows the smallest ohmic resistance of  $160.3 \Omega$  and charge transfer resistance of  $148.4 \Omega$ . While the  $\text{Cu}_2\text{SnS}_3$  cathode shows the largest ohmic and charge transfer resistance of  $783.9$  and  $661.9 \Omega$ , respectively (Table S1, Supporting Information). The super stable  $\text{Cu}_2\text{SnS}_3$ @graphene- $\text{Li}_7\text{P}_3\text{S}_{11}$  cathodes are attributed to uniformly distributed nanoscaled  $\text{Cu}_2\text{SnS}_3$  on graphene and  $\text{Li}_7\text{P}_3\text{S}_{11}$  electrolyte on  $\text{Cu}_2\text{SnS}_3$ @graphene, which ensures uniform electronic/ionic conduction networks, thus resulting in the homogenous and fast reaction of  $\text{Cu}_2\text{SnS}_3$  as well as small and uniform volume change. The uniform volume change will generate small stress/strain, thus less resistance increase during charge/discharge cycles and long cycle life.<sup>[32]</sup> In addition, graphene can also accommodate the expansion and contraction of  $\text{Cu}_2\text{SnS}_3$ , leading to enhanced structural integrity of the solid-state  $\text{Cu}_2\text{SnS}_3$ @graphene- $\text{Li}_7\text{P}_3\text{S}_{11}$ /Li cells. In all-solid-state lithium batteries fabricated by mixing and compressing, the contact between active material and electrolyte is point-to-point contact. The coating  $\text{Li}_7\text{P}_3\text{S}_{11}$  electrolytes on  $\text{Cu}_2\text{SnS}_3$  precipitated graphene change the point-contact to 3D intimate contact in the obtained cathode, which enhance the reaction kinetics and retains integrated morphology and structural robustness of the cathode. Therefore, the best electrochemical performance is realized in all-solid-state lithium batteries using  $\text{Cu}_2\text{SnS}_3$ @graphene- $\text{Li}_7\text{P}_3\text{S}_{11}$  based cathodes.

### 3. Conclusion

$\text{Cu}_2\text{SnS}_3$ @graphene- $\text{Li}_7\text{P}_3\text{S}_{11}$  nanocomposite cathode material with 3D ionic/electronic conduction networks were synthesized by two-step reactions: a hydrothermal process to homogeneously coat  $5\text{--}10 \text{ nm}$   $\text{Cu}_2\text{SnS}_3$  particle on graphene nanosheet followed by in situ liquid-phase deposition of  $\text{Li}_7\text{P}_3\text{S}_{11}$  electrolytes onto  $\text{Cu}_2\text{SnS}_3$ @graphene. The  $\text{Cu}_2\text{SnS}_3$ @graphene- $\text{Li}_7\text{P}_3\text{S}_{11}$  nanocomposite cathode material can maintain the structural integrity, enhance the contact area between electrode material and electrolyte, leading to the decrease of interfacial resistance, and thus endowing the batteries with excellent cycling stability and rate capability. The discharge specific capacity of  $\text{Cu}_2\text{SnS}_3$ @graphene- $\text{Li}_7\text{P}_3\text{S}_{11}$  cathode materials in all-solid-state Li batteries retains at about  $732.0 \text{ mAh g}^{-1}$  at  $100 \text{ mA g}^{-1}$  for 60 cycles, corresponding to a high energy density of  $410.4 \text{ Wh kg}^{-1}$  based on the total mass of cathode layer. At a high current of  $500 \text{ mA g}^{-1}$ ,  $\text{Cu}_2\text{SnS}_3$ @graphene- $\text{Li}_7\text{P}_3\text{S}_{11}$  cathodes can maintain  $363.5 \text{ mAh g}^{-1}$  for 200 cycles. Besides, the  $\text{Cu}_2\text{SnS}_3$ @graphene- $\text{Li}_7\text{P}_3\text{S}_{11}$  nanocomposite also demonstrates extraordinary rate capability of  $964.5$ ,  $813.2$ ,  $706.8$ ,  $540.3$ ,  $466.9$ , and  $359.5 \text{ mAh g}^{-1}$  at current densities of  $50$ ,  $100$ ,  $200$ ,  $500$ ,  $1000$ , and  $2000 \text{ mA g}^{-1}$ , respectively. This study provides a new

route for optimizing the interfacial structure of all-solid-state lithium battery with good rate capability and cycling stability.

## Supporting Information

Supporting Information is available from the Wiley Online Library or from the author.

## Acknowledgements

The work was supported by the funding from the National Key R&D Program of China (Grant No. 2018YFB0905400), National Natural Science Foundation of China (Grant No. 51872303), Zhejiang Provincial Natural Science Foundation of China (Grant No. LD18E020004, LY18E020018), Ningbo S&T Innovation 2025 Major Special Programme (Grant No. 2018B10061, 2018B10087), Natural Science Foundation of Ningbo (Grant No. 2018A610010), and Youth Innovation Promotion Association CAS (2017342).

## Conflict of Interest

The authors declare no conflict of interest.

## Keywords

all-solid-state lithium batteries,  $\text{Cu}_2\text{SnS}_3$ @graphene- $\text{Li}_7\text{P}_3\text{S}_{11}$  nanocomposites, electrochemical performance, electronic/ionic conduction, interfacial architecture

Received: October 12, 2019

Revised: October 28, 2019

Published online: November 14, 2019

- [1] J. G. Kim, B. Son, S. Mukherjee, N. Schuppert, A. Bates, O. Kwon, M. J. Choi, H. Y. Chung, S. Park, *J. Power Sources* **2015**, 282, 299.
- [2] M. H. Chen, X. S. Yin, M. V. Reddy, S. Adams, *J. Mater. Chem. A* **2015**, 3, 10698.
- [3] D. Y. Oh, Y. E. Choi, D. H. Kim, Y.-G. Lee, B.-S. Kim, J. Park, H. Sohnd, Y. S. Jung, *J. Mater. Chem. A* **2016**, 4, 10329.
- [4] X. B. Chen, P. M. Vereecken, *Adv. Mater. Interfaces* **2019**, 6, 1800899.
- [5] Y. Seino, T. Ota, K. Takada, A. Hayashi, M. Tatsumisago, *Energy Environ. Sci.* **2014**, 7, 627.
- [6] Z. C. Liu, W. J. Fu, E. A. Payzant, X. Yu, Z. L. Wu, N. J. Dudney, J. Kiggans, K. L. Hong, A. J. Rondinone, C. D. Liang, *J. Am. Chem. Soc.* **2013**, 135, 975.
- [7] E. Rangasamy, Z. C. Liu, M. Gobet, K. Pilar, G. Sahu, W. Zhou, H. Wu, S. Greenbaum, C. D. Liang, *J. Am. Chem. Soc.* **2015**, 137, 1384.
- [8] N. Kamaya, K. Homma, Y. Yamakawa, M. Hirayama, R. Kanno, M. Yonemura, T. Kamiyama, Y. Kato, S. Hama, K. Kawamoto, A. Mitsui, *Nat. Mater.* **2011**, 10, 682.
- [9] Y. Kato, S. Hori, T. Saito, K. Suzuki, M. Hirayama, A. Mitsui, M. Yonemura, H. Iba, R. Kanno, *Nat. Energy* **2016**, 1, 16030.
- [10] A. C. Luntz, J. Voss, K. Reuter, *J. Phys. Chem. Lett.* **2015**, 6, 4599.
- [11] S. Teragawa, K. Aso, K. Tadanaga, A. Hayashi, M. Tatsumisago, *J. Mater. Chem. A* **2014**, 2, 5095.
- [12] W. Cho, J. Park, K. Kim, J.-S. Yu, G. Jeong, *Small* **2019**, <https://doi.org/10.1002/sml.201902138>.
- [13] Y. Nishio, H. Kitaura, A. Hayashi, M. Tatsumisago, *J. Power Sources* **2009**, 189, 629.
- [14] P. Long, Q. Xu, G. Peng, X. Y. Yao, X. X. Xu, *ChemElectroChem* **2016**, 3, 764.
- [15] Q. Zhang, J. P. Mwirerwa, H. L. Wan, L. T. Cai, X. X. Xu, X. Y. Yao, *J. Mater. Chem. A* **2017**, 5, 23909.
- [16] K. Aso, A. Sakuda, A. Hayashi, M. Tatsumisago, *ACS Appl. Mater. Interfaces* **2013**, 5, 686.
- [17] F. D. Han, J. Yue, X. L. Fan, T. Gao, C. Luo, Z. H. Ma, L. M. Suo, C. S. Wang, *Nano Lett.* **2016**, 16, 4521.
- [18] K. Suzuki, D. Kato, K. Hara, T.-A. Yano, M. Hirayama, M. Hara, R. Kanno, *Electrochim. Acta* **2017**, 258, 110.
- [19] R. P. Fang, G. X. Li, S. Y. Zhao, L. C. Yin, K. Du, P. X. Hou, S. G. Wang, H.-M. Cheng, C. Liu, F. Li, *Nano Energy* **2017**, 42, 205.
- [20] D. Sun, Y. Hwa, Y. Shen, Y. H. Huang, E. J. Cairns, *Nano Energy* **2016**, 26, 524.
- [21] H. L. Wan, G. Peng, X. Y. Yao, J. Yang, P. Cui, X. X. Xu, *Energy Storage Mater.* **2016**, 4, 59.
- [22] Y. Q. Teng, H. L. Zhao, Z. J. Zhang, Z. L. Li, Q. Xia, Y. Zhang, L. Zhao, X. F. Du, Z. H. Du, P. P. Lv, K. Świerczek, *ACS Nano* **2016**, 10, 8526.
- [23] C. M. Chen, Y. C. Yang, X. Tang, R. H. Qiu, S. Y. Wang, G. Z. Cao, M. Zhang, *Small* **2019**, 15, 1804740.
- [24] X. Y. Yao, N. Huang, F. D. Han, Q. Zhang, H. L. Wan, J. P. Mwirerwa, C. S. Wang, X. X. Xu, *Adv. Energy Mater.* **2017**, 7, 1602923.
- [25] X. Y. Yao, D. Liu, C. S. Wang, P. Long, G. Peng, Y. S. Hu, H. Li, L. Q. Chen, X. X. Xu, *Nano Lett.* **2016**, 16, 7148.
- [26] H.-C. Tao, S.-C. Zhu, X.-L. Yang, L.-L. Zhang, S.-B. Ni, *J. Electroanal. Chem.* **2016**, 760, 127.
- [27] Z. A. Zhang, C. K. Zhou, M. Jia, Y. Fu, J. Li, Y. Q. Lai, *Electrochim. Acta* **2014**, 143, 305.
- [28] X. F. Du, H. L. Zhao, Y. Lu, Z. J. Zhang, A. Kulka, K. Świerczek, *Electrochim. Acta* **2017**, 228, 100.
- [29] F. Tuinstra, J. L. Koenig, *J. Chem. Phys.* **1970**, 53, 1126.
- [30] M. Zhang, D. N. Lei, X. Z. Yu, L. B. Chen, Q. H. Li, Y. G. Wang, T. H. Wang, G. Z. Cao, *J. Mater. Chem.* **2012**, 22, 23091.
- [31] S. Stankovich, D. A. Dikin, R. D. Piner, K. A. Kohlhaas, A. Kleinhammes, Y. Jia, Y. Wu, S. T. Nguyen, R. S. Ruoff, *Carbon* **2007**, 45, 1558.
- [32] H. Tavassol, E. M. C. Jones, N. R. Sottos, A. Gewirth, *Nat. Mater.* **2016**, 15, 1182.